Modelling the depth-dependent VASO and BOLD responses in human primary visual cortex

Atena Akbari[1], Saskia Bollmann[1], Tonima S Ali[2], and Markus Barth[1, 3, 4]

[1]Centre for Advanced Imaging, University of Queensland, Brisbane, Australia

[2]School of Biomedical Engineering, The University of Sydney, Sydney, Australia

[3]ARC Training Centre for Innovation in Biomedical Imaging Technology, The University of Queensland, Brisbane, Australia

[4]School of Information Technology and Electrical Engineering, The University of Queensland, Brisbane, Queensland, Australia

Abstract

Functional magnetic resonance imaging (fMRI) using blood-oxygenation-level-dependent (BOLD) contrast is a common method for studying human brain function non-invasively. Gradient-echo (GRE) BOLD is highly sensitive to the blood oxygenation change in blood vessels; however, the signal specificity can be degraded due to signal leakage from the activated lower layers to the superficial layers in depth-dependent (also called laminar or layer-specific) fMRI. Alternatively, physiological variables such as cerebral blood volume using VAscular-Space-Occupancy (VASO) measurements have shown higher spatial specificity compared to BOLD. To better understand the physiological mechanisms (e.g., blood volume and oxygenation change) and to interpret the measured depth-dependent responses we need models that reflect vascular properties at this scale. For this purpose, we adapted a “cortical vascular model” previously developed to predict the layer-specific BOLD signal change in human primary visual cortex to also predict layer-specific VASO response. To evaluate the model, we compared the predictions with experimental results of simultaneous VASO and BOLD measurements in a group of healthy participants. Fitting the model to our experimental findings provided an estimate of CBV change in different vascular compartments upon neural activity. We found that stimulus-evoked CBV changes mainly occur in intracortical arteries as well as small arterioles and capillaries and that the contribution from venules is small for a long stimulus (~30 sec). Our results confirm the notion that VASO contrast is less susceptible to large vessel effects compared to BOLD.

Keywords

Laminar fMRI, VASO, BOLD, cerebral blood volume, cortical layers, primary visual cortex, depth-dependent

1 Introduction

High-resolution functional magnetic resonance imaging (fMRI) offers the potential to measure depth-dependent hemodynamic responses, which can provide insights into cortical information processing and microcircuits of the human brain (Douglas et al., 2004; Lawrence et al., 2019; Stephan et al., 2017). Numerous studies have investigated the function of cortical layers using the blood-oxygenation-level-dependent (BOLD) contrast (Ogawa et al., 1990) in animals and humans (Chen et al., 2013; Goense et al., 2012; Goense et al., 2006; Koopmans et al., 2010; Polimeni et al., 2010; Poplawsky et al., 2015; Ress et al., 2007; Silva et al., 2002; Yu et al., 2014). Despite the high sensitivity of this technique, it suffers from limited specificity due to signal leakage in draining veins carrying blood from (activated) lower layers to superficial layers (Duvernoy et al., 1981; Kim et al., 1994; Turner, 2002). This low specificity was the motivation to develop non-BOLD contrast mechanisms, such as cerebral-blood-volume (CBV) imaging, which is expected to be predominantly sensitive to hemodynamic responses in the microvasculature (Gagnon et al., 2015; Vanzetta et al., 2005).

A non-invasive method for CBV imaging is vascular-space-occupancy (VASO) (Lu et al., 2003), which takes advantage of the difference in blood and tissue T_1 to image the tissue signal while the blood signal is nulled (Huber, 2014; Lu et al., 2003). Since the development of this contrast and its translation to 7T (Huber et al., 2014), several studies in animals and humans have been conducted in the areas of method development (Beckett et al., 2019; Chai et al., 2019; Huber, 2011), analysis strategies (Huber et al., 2020; Polimeni et al., 2018), and applications to cognitive neuroscience (Finn et al., 2019; Kashyap et al., 2016; Van Kerkoerle et al., 2017). However, to interpret the experimental results and account for both neural and vascular contributions to the fMRI signal, detailed models are required (Buxton et al., 2004). Several studies have modelled the BOLD response for both low- and high-resolution acquisitions (Buxton et al., 2004; Buxton et al., 1998; Genois et al., 2020; Havlicek et al., 2019; Heinzle et al., 2016; Markuerkiaga et al., 2016; Uludağ et al., 2009). Given the potential of VASO imaging for layer fMRI, we set out to model the depth-dependent VASO signal changes employing a detailed model of the underlying macro- and microvasculature (Markuerkiaga et al., 2016).

In this work, we adapted the recently developed "cortical vascular model" (Markuerkiaga et al., 2016) to simulate VASO responses in addition to BOLD responses at the laminar level. This model is based on histological observations in monkey's primary visual cortex and considers various vascular features, such as vessel diameter, length, density, and distribution to simulate intra- and extra-vascular BOLD and VASO signals across cortical layers. We added intra-cortical (diving) arteries (ICAs) to the modelled region, as it is hypothesized that these play a role in the functional VASO response based on previous observations (Gagnon et al., 2015; Vanzetta et al., 2005). To fit the predictions of the now extended model to experimental data, we performed simultaneous BOLD and VASO imaging in a group of healthy participants with sub-millimetre resolution at 7T. The model fitting then provides estimates of CBV and oxygenation changes in microvascular (arterioles, capillaries, venules) and macrovascular (ICAs and intracortical veins (ICVs)) compartments at each cortical depth. Furthermore, we investigated the sensitivity of both VASO and BOLD contrasts to changes in the underlying physiological parameters, i.e., CBV and oxygenation. We found that both arterioles and capillaries as well as ICAs show considerable increase in CBV. A surprisingly wide range of CBV changes in the different micro- and macro-vascular compartments can result in similar depth-dependent profiles, indicating potential challenges when aiming to invert the measured profiles. Our results also suggest that the VASO contrast is less sensitive to the large blood vessels compared to BOLD, probably due to its linear relationship with CBV.

In the following section, we briefly summarize the general structure of the previously developed cortical vascular model (2.1 and 2.2), and then describe the applied changes to simulate the VASO and BOLD responses (2.3).

2 Theory and Simulations

2.1 The cortical vascular model

The cortical vascular model developed by Markuerkiaga et al. (2016) simulates the steady-state BOLD response in a depth-dependent manner in human primary visual cortex. The model divides the brain vasculature into two groups: (i) the microvasculature forming a network of randomly oriented arterioles, capillaries, and venules also called the laminar network; and (ii) the macrovasculature in the form of

intracortical veins (ICVs) that drain the microvasculature towards the cortical surface. The vessel distribution in the laminar network is 21% arterioles, 36% capillaries, and 43% venules (Boas et al., 2008). The model investigates the effect of the ascending veins on the BOLD signal by calculating the diameter, blood velocity, and mass flux of the ICVs in each layer. To simulate the VASO response, diving arteries need to be added to the modelled region, as several studies have shown that dilation mainly occurs in arteries and arterioles (Gagnon et al., 2015; Kim et al., 2011b; Vanzetta et al., 2005). To do so, a vascular unit centered on two adjacent principal veins (V3 and V4), surrounded by an arterial ring is modelled in this work with an artery – vein ratio of 2 – 1 (Francis et al., 2009; Lauwers et al., 2008). Figure 1A shows a schematic of the modelled intracortical arteries and veins following Duvernoy et al. (1981), in which vessels are categorized based on their diameter and penetration depth.

The diameter of the intracortical vessels in each depth is calculated following the steps described in Markuerkiaga et al. (2016). In brief, based on the mass conservation law, the incoming mass flux (p) to the arteries should be equal to the outgoing flux from the veins in the modelled region at steady state. Similarly, the mass flux from each depth is the mass flux from within the microvasculature plus the mass flux in the macrovasculature from the previous layer. In general, the mass flux through vessels can be calculated as:

$$p = r^2 \cdot v, \qquad \text{Equation 1}$$

where r is the vessel radius and v is the blood velocity. We can rewrite this as:

$$p = \frac{d^3}{4} \cdot \alpha, \qquad \text{Equation 2}$$

assuming a linear relationship between vessel diameter d and blood velocity (Zweifach et al., 1977):

$$\alpha = \frac{v}{d}. \qquad \text{Equation 3}$$

The mass flux p through a single capillary is calculated assuming d = 8 µm and v = 1.6 mm/s (Boas et al., 2008; Zweifach et al., 1977). Then, p through ICVs and ICAs present in each layer is calculated starting from the layer closest to the white-matter (WM) border based on the number of capillaries in that layer:

$$p_{\mathrm{ICVs}} = \frac{N_{\mathrm{cap}}}{N_{\mathrm{ICVs}}} \cdot p_{\mathrm{cap}}. \qquad \text{Equation 4}$$

For the rest of the layers, p in each layer is the summation of the mass flux within that layer and the mass flux from the previous layer(s). The same calculation for ICVs applies for ICAs, but with twice the number of arteries (Schmid et al., 2017). The α values in pre- and post-capillaries compartments were calculated assuming $d = 8\,\mu m$ and $v = 2\,mm/sec$ in post-capillary and $v = 4\,mm/sec$ in the pre-capillary segment of the vasculature (Zweifach et al., 1977). Then, based on the mass flux for each vessel at each layer, the vessel diameter and the blood velocity of the macrovasculature can be calculated using Equation 2 and Equation 3. Table 1 shows the estimated diameters of intracortical arteries and veins, which are in line with the values reported in Duvernoy et al. (1981).

The baseline blood volume of the laminar network taken from Weber et al. (2008) was interpolated to the number of voxels being simulated, resulting in 2-2.7% baseline CBV (Figure 1B). The intracortical baseline CBV is calculated as:

$$\mathrm{CBV}_{\mathrm{ICAs,ICVs}}^{\mathrm{baseline}} = \pi \frac{d^2}{4} / l^2, \qquad \text{Equation 5}$$

in which l is the simulated voxel length (0.75 mm) yielding a baseline CBV in ICVs ranging from 0.2-1.45% and a baseline CBV in ICAs ranging from 0.17-1.15% (Figure 1C). The total baseline blood volume of the modelled vasculature including the laminar network, ICAs and ICVs is ranging from 2.78 to 4.61% (Figure 1D). These values are in agreement with Barrett et al. (2012), who, based on human and primate data, estimated that arteries make up ~29% of total blood volume, and veins contribute ~27%. This vascular model is then combined with the MR signal model (see section 2.2) to calculate the layer-dependent signal changes.

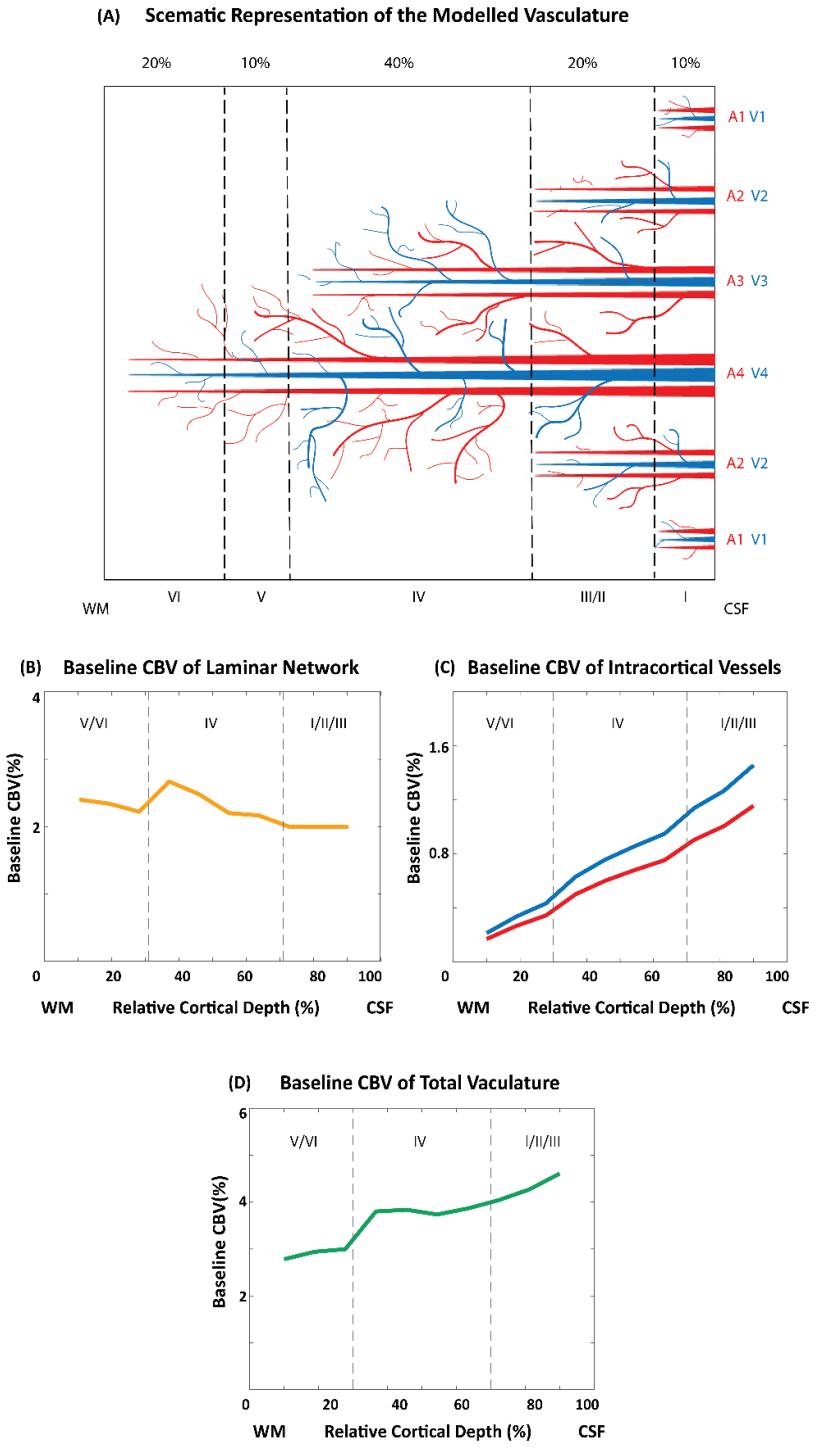

155

156 Figure 1: Vascular model of intracortical vessels and baseline cerebral blood volume of the different
157 vascular compartments. A) Schematic of the vascular features of the primary visual cortex illustrating
158 the 2 – 1 artery – vein ratio. B) Baseline blood volume of the laminar network (i.e., arterioles, capillaries,
159 venules) as a function of cortical depth following Weber et al. (2008). C) Estimated baseline blood
160 volume of the intracortical vessels (ICAs and ICVs). D) Estimated baseline blood volume of the total
161 vasculature.

162

Table 1. The average diameter (in μm) of intracortical arteries and veins in the modelled vascular unit centred on two intermediate-sized veins (V3 and V4) and surrounded by four intermediate-sized arteries (two A3 and two A4). For reference, the ICV diameters of group 1 to 4 reported in Duvernoy et al. (1981) range from 20 to 65 μm, and the diameter of the corresponding ICAs range from 10 to 40 μm.

	V4	***V3***	***V2***	***V1***	***A4***	***A3***	***A2***	***A1***
Layer I	68.6	53.2	32.1	20.2	43.2	33.5	20.2	12.7
Layer II/III	67.5	51.5	26.1		42.6	32.4	16.5	
Layer IV	62.2	41.5			39.5	26.1		
Layer V	55.6				35.1			
Layer VI	44.0				27.7			

2.2 BOLD and VASO MR signal models

The MR signal model employed here is a steady state model contrasting signal levels at baseline and during activity (Markuerkiaga et al., 2016; Uludağ et al., 2009). At baseline, the total MR signal $S_{\text{total}}^{\text{base}}$ is the sum of the intra-(IV) and extra-vascular (EV) signal components (Buxton, 2009; Obata et al., 2004; Uludağ et al., 2009):

$$S_{\text{tot,base}} = (1 - \text{CBV}) \cdot S_{\text{EV,base}} + \sum_i S_{\text{IV,base},i} \cdot \text{CBV}_i, \qquad \text{Equation 6}$$

where CBV is the baseline blood volume, and i denotes different vascular compartments, i.e., arterioles, capillaries, venules, ICVs and ICAs. In the following, we describe the intra- and extra-vascular BOLD and VASO signals when using a GRE readout at 7T.

The BOLD signal is approximated as a mono-exponential decay (Yablonskiy et al., 1994), where TE is the echo time, S_0 the effective spin density at $TE = 0$, and R_2^* the transverse relaxation rate:

$$S^{\text{BOLD}} = S_0 \cdot e^{-TE \cdot R_2^*}. \qquad \text{Equation 7}$$

The transverse relaxation rate is the sum of the intrinsic ($R^*_{2,0}$) and hemoglobin (Hb)-induced transverse relaxation rates ($R^*_{2,\mathrm{Hb}}$):

$$R^*_2 = R^*_{2,0} + R^*_{2,\mathrm{Hb}}. \qquad \text{Equation 8}$$

All intrinsic and Hb-induced R^*_2 values used in this model (Blockley et al., 2008; Uludağ et al., 2009) are summarized in Table 2. Extra- and intra-vascular BOLD signals are estimated using their corresponding relaxation rates. In short, the Hb-induced extra-vascular relaxation rate is calculated according to the susceptibility-induced shift at the surface of the vessel depending on the oxygenation level (Y) (Uludağ et al., 2009). The intra-vascular T^*_2 of the ICVs (intrinsic and Hb-induced) are very small at high field (7T and above). Therefore, the intra-vascular signal in veins approaches zero (Uludağ et al., 2009), and the main intra-vascular contribution comes from the arterial and capillary side of the vasculature.

Table 2: The intrinsic and Hb-induced intra- and extra-vascular transverse relaxation rates used in the BOLD signal model.

	Intrinsic	Hb-induced
Intravascular (blood)	$\boldsymbol{R^*_{2,IV,0}}$ (s^{-1})	$\boldsymbol{R^*_{2,IV,Hb}}$ (s^{-1})
	67	$C \cdot (1-Y)^2$
Extravascular(tissue)	$\boldsymbol{R^*_{2,EV,0}}$ (s^{-1})	$\boldsymbol{R^*_{2,EV,Hb}}$ (s^{-1})
	33.95	$R^*_{2,EV,Hb} = (e \cdot \Delta\nu_s + f) \cdot CBV_i$ $\Delta\nu_s = \frac{\Delta\chi}{4\pi} \cdot Hct \cdot (\lvert Y_{\mathrm{off}} - Y \rvert) \cdot \gamma \cdot B_0$

C: constant that depends on the magnetic field strength (= 536.48).

$\Delta\nu$: the susceptibility-induced shift at the surface of the vessel corresponds to Larmor frequency shift (depends on Y).

$\Delta\chi$: the susceptibility of blood with fully deoxygenated blood (= 3.32).

$\mathrm{Y_{off}}$: the oxygenation level that produces no magnetic susceptibility difference between intravascular and extra-vascular fluids (= 95%).

$e = 0.0453\ and\ f = -0.19$: fitting coefficients.

Following neural activity and changes in blood volume and oxygenation, the total MRI signal is:

$$S_{\mathrm{total,act}} = \left(1 - (\mathrm{CBV} + \Delta\mathrm{CBV}_{\mathrm{act}})\right) \cdot S_{\mathrm{EV,act}} + \sum_i S_{\mathrm{IV,act}} \cdot \left(\mathrm{CBV} + \Delta\mathrm{CBV}_{\mathrm{act},i}\right), \quad \text{Equation 9}$$

where $\Delta\mathrm{CBV}$ is the blood volume change upon activation. The increase in oxygenation is reflected in the shortening of the relaxation rates, which leads to increased extra- and intravascular signal levels. The BOLD signal change in percent (%) following neural activity can be described as the signal difference between baseline and activation, normalized to the baseline signal level:

$$\frac{\Delta S}{S_{base}} = \frac{S_{tot,act} - S_{tot,base}}{S_{tot,base}} \cdot 100\ [\%], \quad \text{Equation 10}$$

For VASO, signal change arises only from the extravascular component, as the intravascular signal is nulled with an inversion pulse. The steady state nulled tissue signal is (Lu et al., 2003):

$$S_{EV}^{nulled} = \mathrm{S_0}\left(1 - (1+\varepsilon)\mathrm{e}^{\frac{-\mathrm{TI}}{\mathrm{T_1}}} + \varepsilon\mathrm{e}^{\frac{-\mathrm{TR}}{\mathrm{T_1}}}\right) \cdot \mathrm{e}^{-\mathrm{TE}\cdot\mathrm{R}_{2,\mathrm{EV}}^{*}}, \quad \text{Equation 11}$$

in which ε is the inversion efficiency (here assumed to be equal to 1), $TI/T_1/TR$ are the blood nulling time, longitudinal relaxation time, and repetition time, respectively. At the time of the blood nulling, a BOLD signal contamination — the T_2^*-dependency — is still present and needs to be corrected. The dynamic division approach proposed by Huber et al. (2014) removes the T_2^*-contribution from the VASO signal by dividing the "nulled" by the "non-nulled" signal, assuming equal BOLD contributions in both images:

$$S_{\mathrm{EV}}^{\mathrm{VASO}} = \frac{S_{\mathrm{EV}}^{\mathrm{nulled}}}{S_{\mathrm{EV}}^{\mathrm{non-nullded}}} = \mathrm{S_0}\left(1 - (1+\varepsilon)\cdot\mathrm{e}^{\frac{TI}{T_1}} + \varepsilon\cdot\mathrm{e}^{\frac{-\mathrm{TR}}{T_1}}\right) \quad \text{Equation 12}$$

Then, the VASO signal during baseline, activity, and total VASO signal change can be derived from Equation 6, Equation 9, and Equation 10 by considering only the extravascular components:

$$S_{\mathrm{tot,base}}^{\mathrm{VASO}} = (1 - \mathrm{CBV}) \cdot S_{\mathrm{EV}}^{\mathrm{VASO}}$$
$$S_{\mathrm{tot,act}}^{\mathrm{VASO}} = [1 - (\mathrm{CBV} + \Delta\mathrm{CBV})] \cdot S_{\mathrm{EV}}^{\mathrm{VASO}} \qquad \text{Equation 13}$$
$$\frac{\Delta S^{\mathrm{VASO}}}{S_{\mathrm{base}}^{\mathrm{VASO}}} = \frac{-\Delta CBV}{1 - CBV}.$$

Thus, VASO signal changes are only a function of CBV change, and independent of oxygenation changes.

2.3 Model Assumptions and Simulations

To simulate depth-dependent BOLD and VASO signal changes, the cortical vascular model outlined in section 2.1 requires ΔCBV and oxygenation values at baseline and activity for each depth and vascular compartment. Note that ΔCBV here is given in percent of the baseline CBV, i.e., an increase of 100 % means that CBV during activation is twice as large as during baseline. Further, oxygenation is given in percent oxygen saturation, with 100% oxygenation corresponding to fully oxygenated blood. The resulting BOLD and VASO profiles are presented in percent signal change following equation Equation 10 and Equation 13.

To find the input values that best fit the empirical data (see section 3.2), we simulated numerous profiles for a wide range of input parameters (Table 3), and then calculated the root-mean-squared-error (RMSE) for each simulated profile with the experimental result. The minimum RMSE value indicates the highest similarity between simulated and measured depth-dependent responses. To investigate the effect of input parameters on the resulting depth-dependent profiles, we also plotted the range of profiles obtained with an RMSE 20% higher than the minimum RMSE and extracted the corresponding input values for ΔCBV and oxygenation. For reference, we have included the original values used in Markuerkiaga et al. (2016) in square brackets in Table 3.

To account for partial volume effects across layers and provide a better comparison between simulated and measured depth-dependent responses (Markuerkiaga et al., 2016), we applied a smoothing kernel (Koopmans et al., 2011) to the simulated

profiles. The resulting zero-padded edges of the laminar profiles were thus excluded from the RMSE estimation, and only the central eight data points contributed.

In the original version of the cortical vascular model, Markuerkiaga et al. (2016) assumed the same increase in CBV of 16.6% (Griffeth et al., 2015) in each compartment of the laminar network across all depths. Using these input values, the resulting depth-dependent VASO signal change (see Figure 7) did not exhibit the characteristic peak in the middle layers observed in our and other VASO experiments (Huber et al., 2013). We therefore assumed a non-uniform CBV change across layers. For the VASO simulations, we assumed in the laminar network a 1.5 times higher CBV increase in middle cortical layers (IV) compared with deep (V and VI) and superficial (I and II/III) layers following the ratio reported in Weber et al. (2008). In ICAs, we assumed higher CBV change in middle and upper cortical layers compared with the lower depths (see Figure 2). We then simulated VASO profiles using this ratio for a range of ΔCBV values in the middle layers of 0 - 150 % for ICAs, arterioles, capillaries, and venules (Table 3). Note that we mostly let the ΔCBV vary independently between the vascular compartments, but followed the original implementation considering arterioles and capillaries jointly. In addition, we assumed that the CBV change occurs exclusively in ICAs and the laminar network, and $\Delta\mathrm{CBV}$ in ascending veins remains negligible.

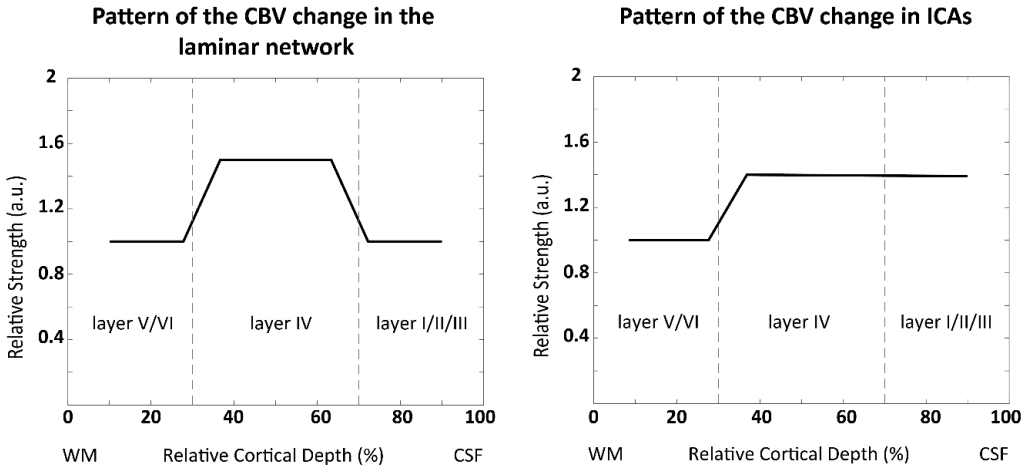

Figure 2: The pattern of the CBV change in the laminar network (left) and ICAs (right) across the layers used in our simulations. Following (Weber et al., 2008) we assumed that CBV change in superficial and deep layers is 2/3 of the CBV change in middle layers in the laminar network. In ICAs, the assumption is that the CBV change in deep layers is 2/3 of the change in middle and superficial layers.

For the BOLD simulations, we used the ΔCBV values of the best fit from the VASO experiment, and instead varied oxygenation values between 60-75% at baseline and 75-90% at activation in the venules and ICVs (see Table 1). Following Markuerkiaga et al. (2016) and Uludağ et al. (2009), we assumed that ICAs, arterioles, and capillaries are mostly oxygenated at baseline, and kept their oxygenation values fixed across simulations. Again, we compared the resulting profiles to the experimental BOLD data to obtain those input parameters that provided the best fit.

Table 3: The range of the model parameters for simulating VASO and BOLD depth-dependent responses. Note that in the VASO simulations, we assumed that CBV change in arterioles and capillaries is the same, but different from venules and ICAs, however the oxygenation change in vascular components was considered to be different. The values in brackets refer to the values used in the original vascular model. Y_{base} and Y_{act} are the blood oxygenation at baseline and activation, and ΔCBV_{mid} refers to the CBV change in middle layers which is 1.5 times higher than CBV change in deep and superficial layers.

	Vascular Compartment				
	arterioles	**capillaries**	**venules**	**ICVs**	**ICAs**
$\boldsymbol{Y_{base}}$	95% [95 %]	85% [85%]	60- 75*% [60%]	60-75*% [60%]	95% --
$\boldsymbol{Y_{act}}$	100% [100%]	95% [95%]	75-90†% [70%]	75-90†% [70%]	100% --
$\boldsymbol{\Delta CBV_{mid}}$	0–150% [16.6%]	0-150% [16.6%]	0-150% [16.6%]	0% 0%	0-150% --

*Corresponds to $R^*_{2,IV} = 100.53 - 152.84\ sec^{-1}$
†Corresponds to $R^*_{2,IV} = 72.37 - 100.53\ sec^{-1}$

3 Experimental Methods

3.1 Model Implementation

The cortical vascular model was implemented in MATLAB (2018b, The MathWorks, Inc.). The code is available on gitlab (https://gitlab.com/AtenaAkbari/cortical-vascular-model) including the original version used in Markuerkiaga et al. (2016) (branch: originalCode), the implementation used for an earlier version of this work presented at the ISMRM 2020 in which intracortical arteries were not yet added (Akbari et al., 2020) (branch: vasoSignal), and the implementation used in this manuscript (branch: master).

3.2 Image Acquisition

Imaging was performed on a 7T whole-body MR scanner (Siemens Healthcare, Erlangen, Germany), with a maximum gradient strength of 70 mT/m and a slew rate of 200 mT/m/s. A single-channel Tx and 32-channel Rx head coil array (Nova Medical, Wilmington, MA, USA) was used for radiofrequency transmission and signal reception. The slice-selective slab-inversion (SS-SI) VASO sequence (Huber et al., 2014) was employed to scan ten healthy participants (2 females; age range 19-32 years) after giving written informed consent according to the approval of the institutional ethics committee. For each subject, BOLD and VASO images were acquired in an interleaved fashion in three runs with 400 volumes in each run (19 minutes total acquisition time per run). The sequence parameters were: volume $TR = 4.5s$, $TE = 25\,ms$, $TI = 650\,ms$, GRAPPA (Griswold et al., 2002) acceleration factor $= 3$, isotropic voxel size $= 0.8$, number of slices $= 26$, partial Fourier in the phase encoding direction $= 6/8$, in combination with a 3D EPI readout (Poser et al., 2010). The blood-nulling time was chosen based on the assumed value of blood T_1 = $2100\,ms$ following earlier VASO studies at 7T (Huber et al., 2015; Huber et al., 2016; Zhang et al., 2013). The effective TI used in the sequence was the summation of the above-mentioned TI and half of the readout duration. The visual stimulus consisted of 17 ON- and OFF-blocks with 30 s duration each. During the ON condition, a flashing black and white noise pattern was presented, and a fixation cross was the OFF condition of the stimulus (Polimeni et al., 2005). The imaging slices were positioned and oriented such

that the center of the imaging slab was aligned with the center of the calcarine sulcus, the part of the striate cortex with the highest vascular density in layer IV (Duvernoy et al., 1981). Whole-brain MP2RAGE images (Marques et al., 2010; O'Brien et al., 2014) were acquired with an isotropic resolution of 0.75 mm for each participant in the same session as the functional imaging.

3.3 Image Analysis

The first volume of each contrast was discarded to ensure T_1 effects were at equilibrium. Dynamic division was then performed to account for the BOLD-contamination (Huber et al., 2014). The BOLD and BOLD-corrected VASO images were motion corrected using SPM12 (Wellcome Department, UK). Activation maps were estimated with the GLM analysis in SPM with no spatial smoothing. Data from three participants were discarded due to excessive motion, i.e., volume-to-volume displacement of more than one voxel size. Voxels with t-values above 2.3 corresponding to an uncorrected significance level of $p < 0.01$ were identified as the activated regions for both BOLD and BOLD-corrected VASO images.

For the layer analysis, we followed the steps outlined in Huber et al. (2014): The $T_1 - EPI$ images of each subject were used for manual WM/GM and GM/CSF boundary delineation. Then, this region-of-interest (ROI) in V1 was used to create ten equi-volume layers (Waehnert et al., 2014) using the open-source LAYNII package (Huber et al., 2020) and extract depth-dependent BOLD and VASO responses. The mean and standard error of the mean were calculated across participants, and average BOLD and VASO responses across all participants were used as a reference when evaluating the model predictions. Note that cortical layers in these analyses refer to a group of voxels obtained by dividing the ROI into 10 equi-volume layers and do not refer to the histological cortical layers. In the next section, we will first present the imaging results, and then introduce the simulations that fit these best. Further, we will present the simulated profiles with an RMSE 20% higher than the minimum RMSE, and the ΔCBV and oxygenation values corresponding to these profiles.

4 Results

4.1 Imaging

The BOLD and VASO activation maps of all seven participants included in this study are shown in Figure 3. We observed overall higher t-values for the BOLD contrast compared to the VASO contrast. Further, highest t-values for BOLD are located at the cortical surface and within various sulci. In contrast, most of the VASO response is confined to the grey matter. An example of the ROI placed on V1 to extract the 10 equi-volume layers and estimate the depth-dependent profiles is shown for one subject in Figure 3.

The depth-dependent BOLD and VASO signal changes for each participant as well as the mean and standard error of the mean of these profiles are shown in Figure 4. On average, we observed a mean signal change of 5.71% for BOLD and 1.07% for VASO, evidence for the larger effect size of the BOLD contrast. In agreement with previous studies, BOLD signal change peaks at the cortical surface (Koopmans et al., 2010; Olman et al., 2012; Polimeni et al., 2010) while the VASO signal change has its maximum in the middle cortical layers (Huber et al., 2013).

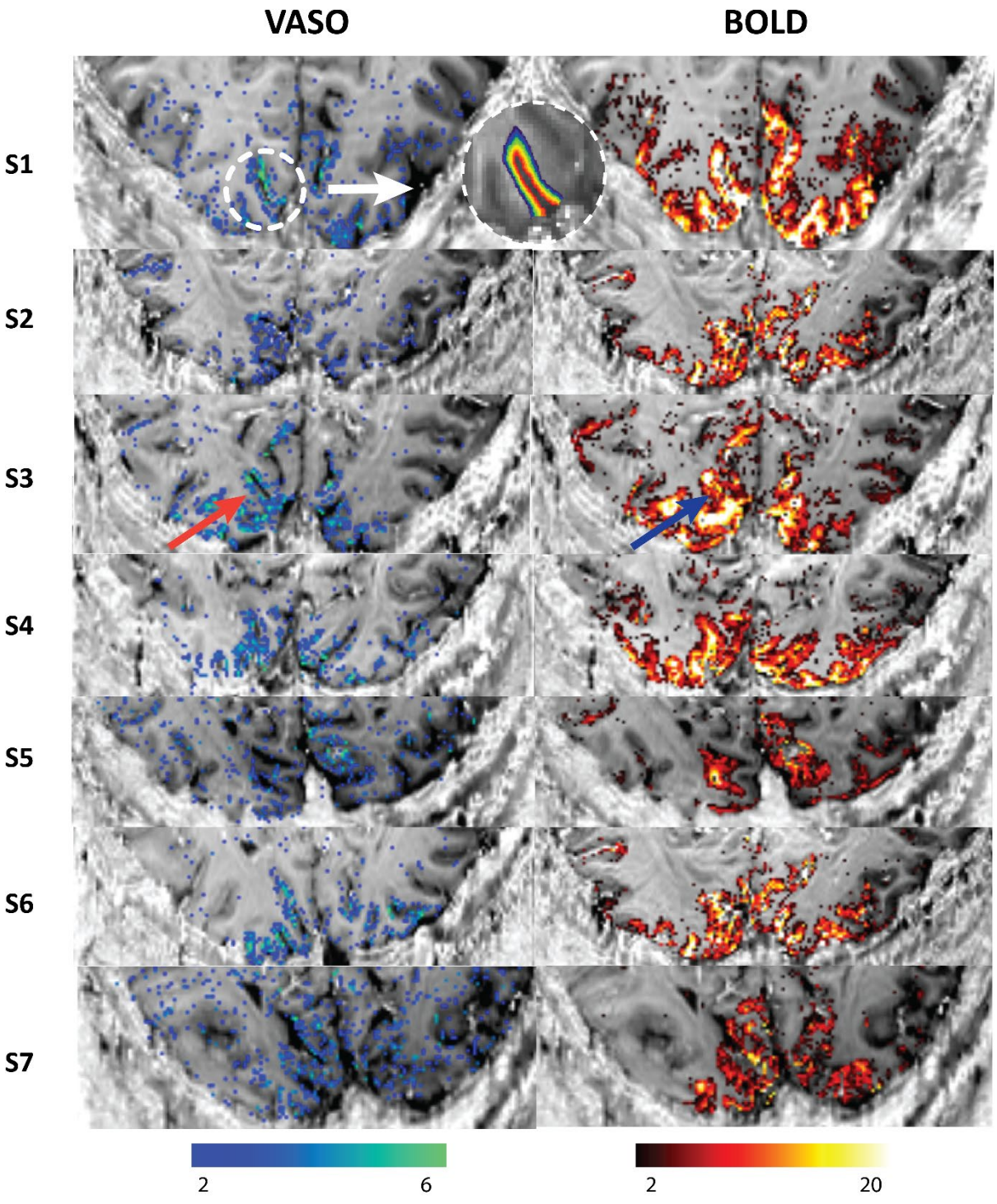

Figure 3: VASO and BOLD statistical activation maps of all participants in our study using the SS-SI VASO sequence (Huber et al., 2015) with an isotropic resolution of 0.8 mm. The activation maps are overlaid on T1-EPI images of each subject. The VASO contrast is more confined to GM while BOLD shows higher activity near surface (indicated with the blue and red arrows). An example of the region-of-interest (ROI) in V1 for the layer analysis is shown above. Ten equi-volume layers were extracted from GM in the T1-EPI images to calculate the mean signal change in each layer.

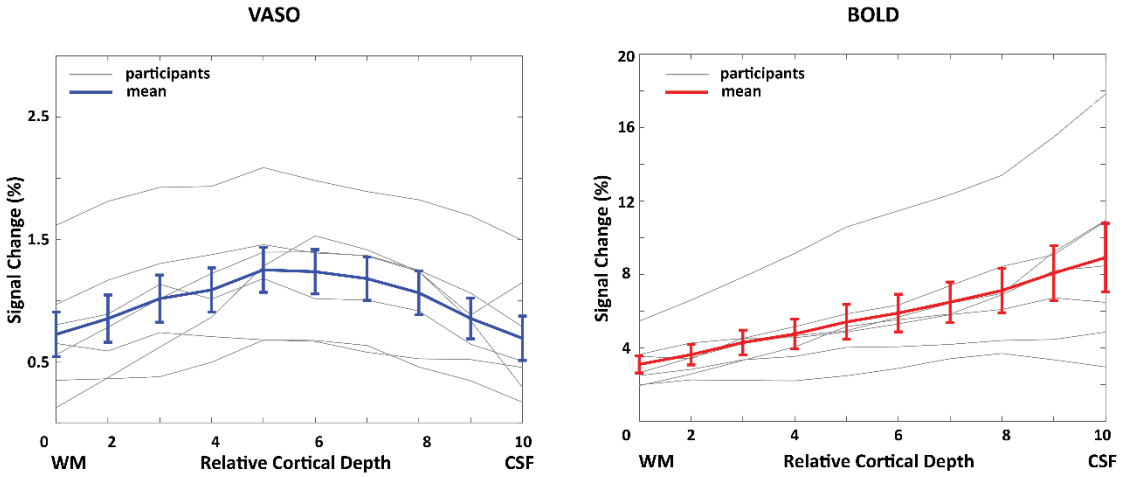

Figure 4: Depth-dependent VASO (absolute values) and BOLD signal changes in human V1 for each individual participant (gray) and averaged across all participants (blue and red). In this and all following graphs error bars refer to the standard error of the mean across all participants.

4.2 Simulations

The simulated VASO profile with the best fit is shown in Figure 5, and corresponding CBV changes are shown in Table 4. These agree with previous studies (Drew et al., 2011; Vanzetta et al., 2005) that have shown lower CBV change in venules compared with the CBV change in arterioles and capillaries when the stimulus duration is long ($> 20\ sec$). Using a Grubb value (Grubb et al., 1974) of 0.35, the corresponding CBF change upon activation in middle layers would be 63.2% in ICAs, 87.1% in arterioles and capillaries, and 49.6% in venules. For BOLD, the simulation with the best-fit yields $Y_{base} = 64\%$ and $Y_{act} = 77\%$ in venules and ICVs. The minimum RMSE of the VASO and BOLD best fits are 0.08 and 1.03, respectively.

Table 4: CBV change in vascular compartments correspond to the best-fit show in Figure 5. The minimum and maximum of the estimated CBV change in the 20% RMSE regime (i.e. the minimum RMSE+20% of the minimum RMSE shown as the shaded area in Figure 5) are shown in brackets.

CBV change in vascular compartments			
Cortical depth	**Arterioles & capillaries**	**venules**	**ICAs**
Deep	**45%** [0% 57%]	**9%** [0% 79%]	**18%** [8% 28%]
Middle	**67.5%** [0% 85%]	**13.5%** [0% 118%]	**27%** [12% 42%]
superficial	**45%** [0% 57%]	**9%** [0% 79%]	**27%** [12% 42%]

To investigate the sensitivity of the model to the choice of input parameters, the shaded area in Figure 5 illustrates the range of profiles with an RMSE up to 20% higher than the minimum RMSE. The resulting profiles remain predominantly within the standard error of the measured profiles. The corresponding input parameter ranges are illustrated in Figure 6, which shows the RMSE values of simulated VASO and BOLD profiles for different input parameter combinations. Note that the input parameters for VASO simulations are ΔCBV in ICAs, arterioles/capillaries, and the venules of the laminar network, and the input for the BOLD simulation are blood oxygenation values (Y) during baseline and activation in the venules of the laminar network and the ICVs. To illustrate the resulting 4D parameter space for VASO, three intersections (2 input parameters + RMSE) at the point of the minimum RMSE are shown. The white dotted lines indicate the range of RMSE values up to 20 % higher than the minimum RMSE. Note how the diagonal band of minimal RMSE values in Figure 6B is contained within this limit, which indicates a large number of possible ΔCBV combinations would result in similar profiles, ranging from no change in CBV in venules but 70 % ΔCBV in arterioles and capillaries, to 100% ΔCBV in venules but no change in CBV of arterioles and capillaries. Smaller regions of minimal RMSE can be found in Figure 6B and Figure 6C, indicating that a narrower range of ΔCBV combinations would give rise to similar profiles for these parameter combinations. The RMSE for the BOLD simulations with varying blood oxygenation values at baseline and during activation is shown in Figure 6D. Again, the diagonal band enclosed by the

20 % RMSE limit indicates that various combinations of blood oxygenation values would result in similar profiles. A ΔY of approximately 18% between baseline and activation yields similar low RMSE values.

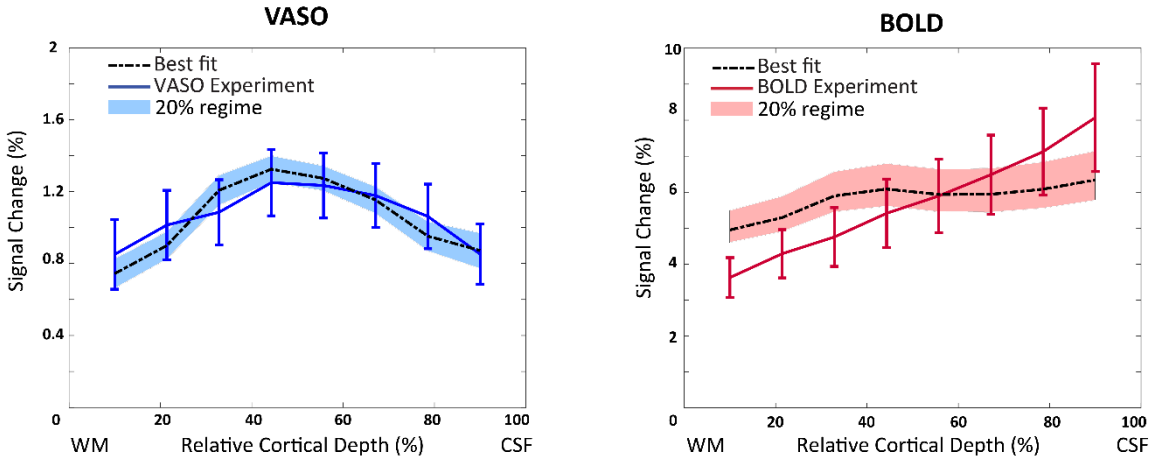

Figure 5: The measured VASO (left) and BOLD (right) profiles and the simulated profiles with the lowest RMSE (black line). Shaded area shows the VASO and BOLD simulated profiles with RMSE 20% higher than the minimum RMSE.

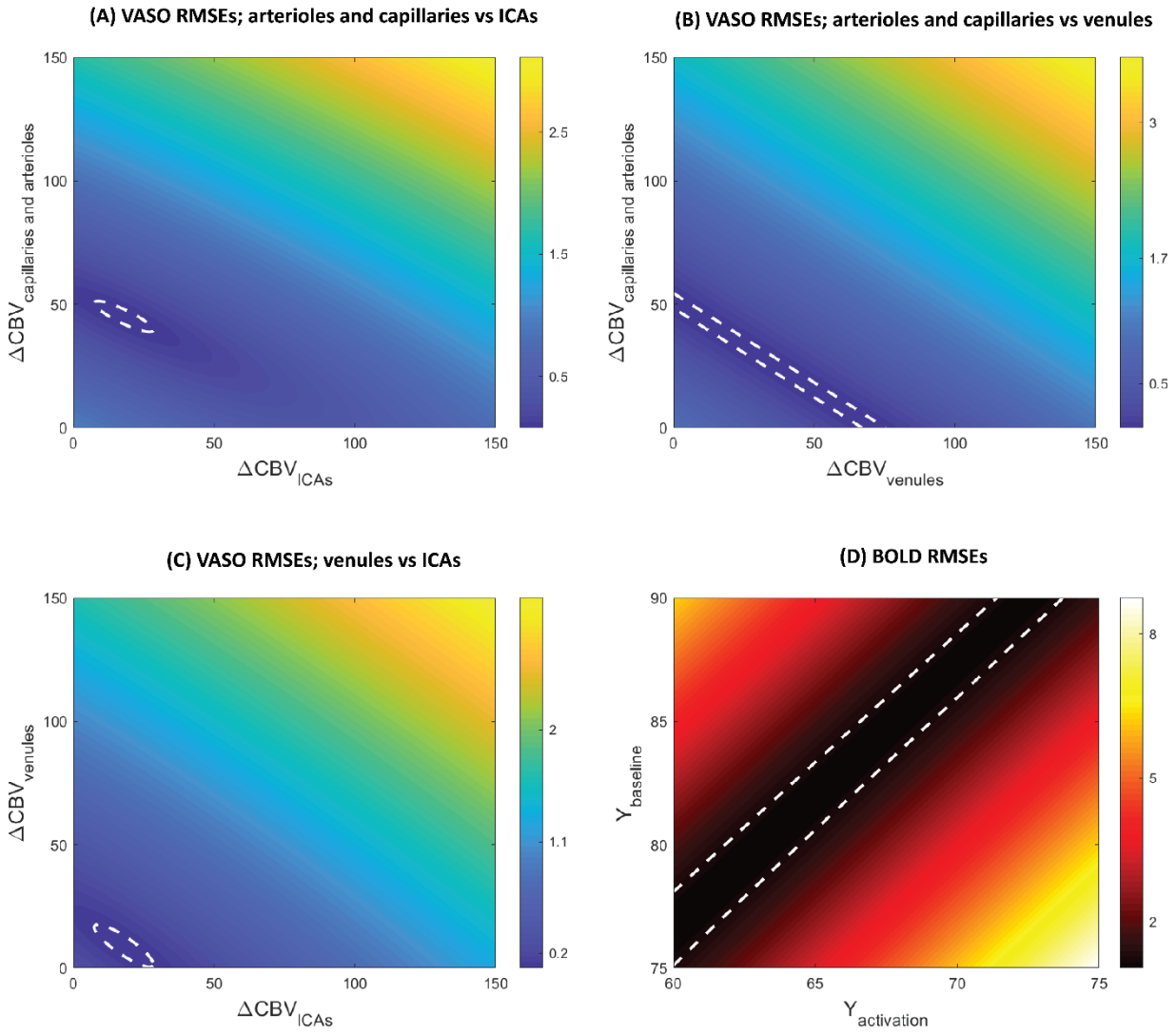

Figure 6: The root-mean-square-error (RMSE) values calculated as a measure of similarity between simulated and measured profiles. The white dotted lines refer to the RMSEs 20% higher than the minimum RMSE. (A) shows the RMSE when varying ΔCBV in arterioles/capillaries and ICAs but keeping the ΔCBV in venules at the value obtained from the profile with minimum RMSE. Similarly, (B) the ΔCBV in arterioles/capillaries and venules is varied but kept constant in the ICAs. (C) the RMSE is shown when varying the ΔCBV in ICAs and venules but using the optimal value for the ΔCBV in capillaries/arterioles. (D) BOLD RMSEs.

The simulation results of equal activation strength across layers, i.e., when all layers are equally activated and CBV change is the same for all vascular compartments as assumed in the original implementation, is shown in Figure 7. With this assumption, the VASO profile is much flatter and does not show higher CBV change in middle layers as expected (Goense et al., 2012; Poplawsky et al., 2014; Zhao et al., 2006)

due to the higher density of capillaries and metabolic responses. The best fit suggests 48% CBV change in arterioles and capillaries, 26% in venules, and 24% in ICAs.

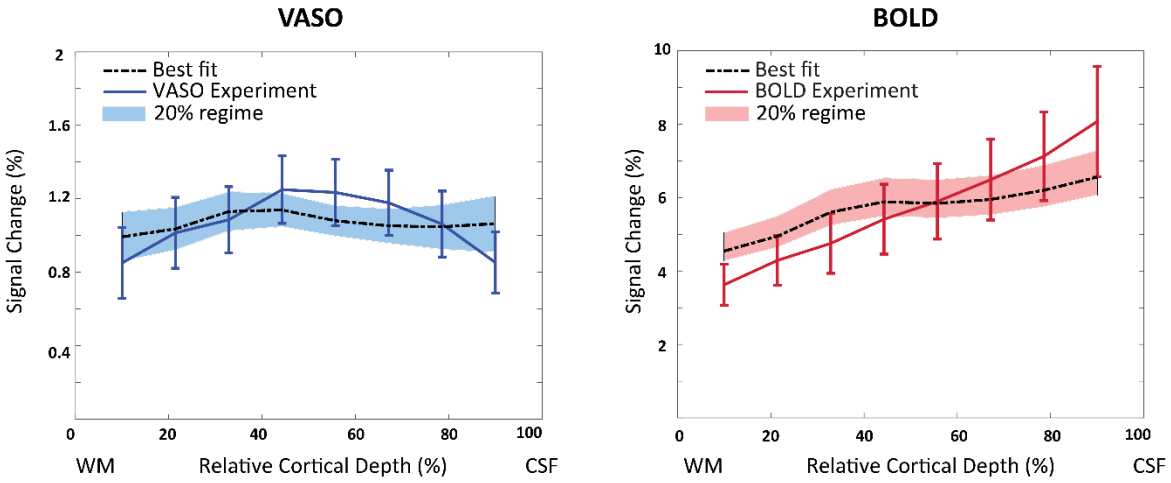

Figure 7: VASO and BOLD simulation results when the activation strength is equal across the layers. With this equal vascular response assumption, the simulated VASO response amplitude does not fit the experimental data well.

Figure 8 shows the uncorrected and BOLD-corrected simulated VASO signals along with the extra- and intra-vascular BOLD signals corresponding to the best fit. The BOLD contamination in the uncorrected VASO manifests as a signal increase near the cortical surface. When correcting for the T_2^*-dependency, the signal change peaks in the middle layers. The small intra-vascular BOLD signal change stems from the more oxygenated blood vessels, i.e., ICAs, arterioles and capillaries, and the extra-vascular BOLD signal increase near the surface is due to the dephasing of the tissue signal around venules and ICVs.

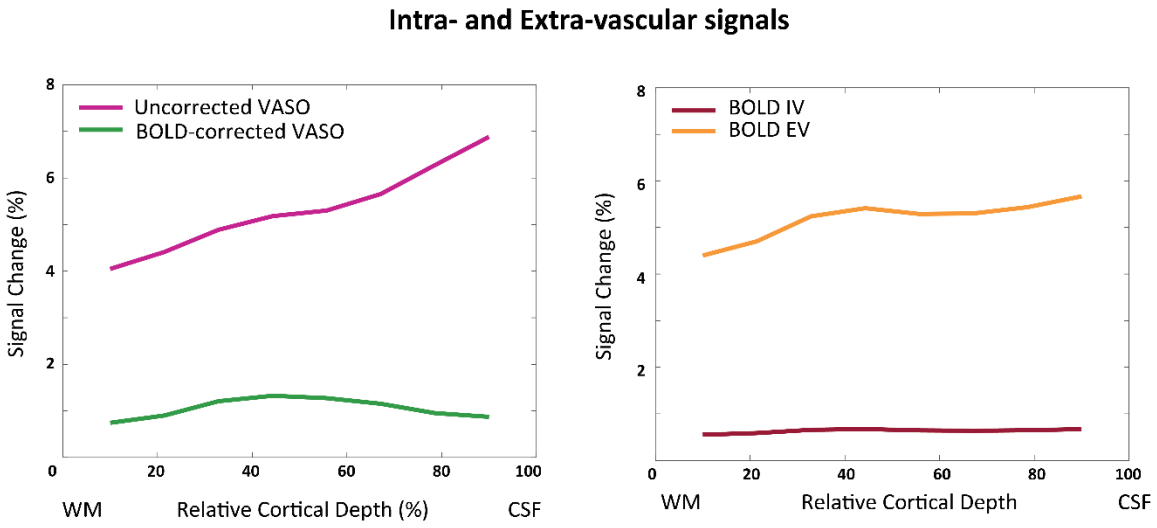

Figure 8: A) the uncorrected and BOLD-corrected simulated VASO profiles corresponding to the best fit. B) intra- and extra-vascular simulated BOLD signal correspond to the best fit.

5 Discussion and Conclusion

In this study, we adapted the cortical vascular model to simulate depth dependent VASO signal change in addition to BOLD signal change and added intra-cortical arteries to the modelled area for a full description of CBV changes in the intra-cortical vasculature. With our simulations, we found that stimulus evoked CBV changes are dominant in small arterioles and capillaries at around 67.5 % in steady state, and the contribution of venules is small at around 13.5 %. These estimates are in line with optical imaging studies performed in rodents, mice, and cats (Drew et al., 2011; Ma et al., 2016; Vanzetta et al., 2005) that reported the highest vascular response in arterioles and capillaries, while veins showed the smallest response. Several MR imaging studies (Gagnon et al., 2015; Hua et al., 2011; Jahanian et al., 2015; Jin et al., 2008b; Kim et al., 2007; Kim et al., 2010; Kim et al., 2011a; Vazquez et al., 2012) also reported higher CBV change in arterioles and smaller change in downstream vessels. The larger CBV change in arterioles and capillaries compared with intracortical arteries in our simulations, is also in line with Drew et al. (2011) and Gao et al. (2015) observations. We also found that a large range of CBV changes in the different vascular compartments resulted in similar CBV profiles (Figure 6), indicating a limited sensitivity of the VASO profile to small differences in CBV change. Overall, the cortical vascular model allows to estimate and compare BOLD and VASO changes in various conditions and resolve the contributions of different vascular compartments.

The inclusion of ICAs allowed us to investigate the sensitivity of the VASO signal to upstream CBV changes. Although we found a relatively large change in CBV of 27 % in ICAs, the measured and simulated profiles did not show the pial bias that is commonly found in BOLD profiles. This might be due to the different contrast mechanisms of VASO and BOLD, where the VASO signal is directly (linearly) proportional to CBV (Equation 13). Together with the low baseline blood volume in ICAs (Figure 1C), even a relatively large change in CBV in ICAs might thus only have a limited impact on the resulting VASO profile. In contrast, the extravascular signal contributions around venules and ICVs presumably amplify the effect of oxygenation changes in these vessels on the BOLD signal. Thus, the measured and simulated BOLD profiles are heavily skewed towards the signal stemming from ICVs. In conclusion, our results indicate that VASO contrast is less susceptible to large vessel effects compared to BOLD.

The various parameters used to build the cortical vascular model such as blood velocity, vessel diameter and baseline blood volume in capillaries were taken from previous research in cats, rabbits, and macaques (Markuerkiaga et al., 2016; Weber et al., 2008; Zweifach et al., 1977). We noticed that for certain parameter combinations the derived vessel diameters and blood velocities in the ICAs and ICVs can easily contradict previous reports that intracortical arteries have smaller diameter (Duvernoy et al., 1981) and fast blood velocities (Zweifach et al., 1977). Thus, while the cortical vascular model aims for a detailed description of the underlying micro- and macro-vasculature and its influence on the MR signal, many uncertainties in the specific parameter choices remain. One example includes the dilation profile of the ICAs across cortical depths, where we assumed a higher vascular response in middle and superficial layers (Figure 2). However, another possible scenario could be an equal vascular response in ICAs across the cortical depths (see the supplementary material), which results in similar depth-dependent VASO and BOLD profiles, but different estimated CBV changes (Figure S2). Additionally, the inter-individual variability in these parameters remains unknown, but may potentially have a large effect on the individual profiles given the many studies showing significant differences in hemodynamic responses between participants (Aguirre et al., 1998; Duann et al., 2002; Handwerker et al., 2004; Light et al., 1993). Consequently, a more detailed understanding of the relative impact of each of these parameters needs to be

developed, in combination with auxiliary image acquisitions that measure relevant underlying parameters (Hua et al., 2019).

The experimental results show similar profiles as expected from previous research (Huber et al., 2013; Huber et al., 2016; Jin et al., 2006, 2008a; Koopmans et al., 2010). To ensure highest contrast-to-noise ratio when comparing with the simulations, we have averaged the responses across participants. We extracted percent signal change values using a GLM, assuming the same hemodynamic response for all cortical layers. Although each layer has a unique HRF (Petridou et al., 2017), we expect a negligible bias in the estimated signal change due to the very long stimulus time employed here. There is also evidence of the dependency of blood T_1 on Hct levels (Dobre et al., 2007) affecting the blood nulling time, though the effect can be considered negligible (Huber, 2011).

The vascular anatomical model used here presents a simplification of vascular anatomical networks (VAN) (Boas et al., 2008; Genois et al., 2020), but employs more details in the mirco- and macro-vasculature than the fully invertible model developed by Havlicek et al. (2019). Thus, it is uniquely suited to translate new insights from detailed VAN models developed in mice to the dynamic laminar models used to fit human data. As exemplified in this work using changes in CBV, the impact of each parameter on the resulting laminar profiles can be assessed individually, to then inform the choice of acquisition, potential vascular biases, and the need for auxiliary information. Next, the vascular anatomical model can be extended to other cortical areas characterized by different vascular properties such as primary motor cortex (Huber et al., 2017), primary somatosensory cortex (Shih et al., 2013; Silva et al., 2002), dorsolateral-prefrontal cortex (Finn et al., 2019), which are currently under active investigation using laminar fMRI to help to understand the vascular and neural signal contributions.

In summary, we acquired BOLD and VASO laminar responses in human V1 at 7T, and simulated these responses using the cortical vascular model. By fitting the model to our experimental results, we obtained an estimate of CBV change in vascular compartments upon neural activity. Our simulation results show that stimulus evoked CBV change is dominant in small arterioles and capillaries and the contribution of venules in total CBV change is small. Our results also suggest that the large vessel bias in BOLD contrast is more prominent compared with VASO, as the BOLD signal

533 relationship with the oxygenation change is exponential, but VASO depends on the
534 CBV change linearly.

535 6 Declaration of interests

536 None.

537 7 Acknowledgement

538 We acknowledge the helpful discussions with and support from Laurentius (Renzo)
539 Huber, Jonathon Polimeni, and Irati Markuerkiaga. We thank Aiman Al-Najjar and
540 Nicole Atcheson for help with data collection. This work was supported by the NHMRC
541 (grant APP1117020) and the NIH (grant R01-MH111419). MB acknowledges funding
542 from ARC Future Fellowship grant FT140100865. AA acknowledges support through
543 the University of Queensland Research Training Program Scholarship. We also
544 acknowledge the facilities and scientific and technical assistance of the National
545 Imaging Facility (NIF), a National Collaborative Research Infrastructure Strategy
546 (NCRIS) at the Centre for Advanced Imaging, the University of Queensland.

547

8 References

Aguirre, G.K., Zarahn, E., D'Esposito, M.J.N., 1998. The variability of human, BOLD hemodynamic responses. 8, 360-369.

Akbari, A., Bollmann, S., Ali, T., Barth, M., 2020. Modelling the Laminar VASO Signal Change in Human V1 at 7T. 28th Annual Meeting of the International Society for Magnetic Resonance Imaging in Medicine.

Barrett, M.J., Tawhai, M.H., Suresh, V.J.N., 2012. Arteries dominate volume changes during brief functional hyperemia: evidence from mathematical modelling. 62, 482-492.

Beckett, A.J., Dadakova, T., Townsend, J., Huber, L., Park, S., Feinberg, D.A.J.b., 2019. Comparison of BOLD and CBV using 3D EPI and 3D GRASE for cortical layer fMRI at 7T. 778142.

Blockley, N., Jiang, L., Gardener, A., Ludman, C., Francis, S., Gowland, P.J.M.R.i.M.A.O.J.o.t.I.S.f.M.R.i.M., 2008. Field strength dependence of R1 and R relaxivities of human whole blood to prohance, vasovist, and deoxyhemoglobin. 60, 1313-1320.

Boas, D.A., Jones, S.R., Devor, A., Huppert, T.J., Dale, A.M., 2008. A vascular anatomical network model of the spatio-temporal response to brain activation. Neuroimage 40, 1116-1129.

Buxton, R.B., 2009. Introduction to functional magnetic resonance imaging: principles and techniques. Cambridge university press.

Buxton, R.B., Uludağ, K., Dubowitz, D.J., Liu, T.T., 2004. Modeling the hemodynamic response to brain activation. Neuroimage 23, S220-S233.

Buxton, R.B., Wong, E.C., Frank, L.R.J.M.r.i.m., 1998. Dynamics of blood flow and oxygenation changes during brain activation: the balloon model. 39, 855-864.

Chai, Y., Li, L., Huber, L., Poser, B.A., Bandettini, P.A.J.N., 2019. Integrated VASO and perfusion contrast: A new tool for laminar functional MRI. 116358.

Chen, G., Wang, F., Gore, J.C., Roe, A.W.J.N., 2013. Layer-specific BOLD activation in awake monkey V1 revealed by ultra-high spatial resolution functional magnetic resonance imaging. 64, 147-155.

Dobre, M.C., Uğurbil, K., Marjanska, M.J.M.r.i., 2007. Determination of blood longitudinal relaxation time (T1) at high magnetic field strengths. 25, 733-735.

Douglas, R.J., Martin, K.A., 2004. Neuronal circuits of the neocortex. Annu. Rev. Neurosci. 27, 419-451.

Drew, P.J., Shih, A.Y., Kleinfeld, D.J.P.o.t.N.A.o.S., 2011. Fluctuating and sensory-induced vasodynamics in rodent cortex extend arteriole capacity. 108, 8473-8478.

Duann, J.-R., Jung, T.-P., Kuo, W.-J., Yeh, T.-C., Makeig, S., Hsieh, J.-C., Sejnowski, T.J.J.N., 2002. Single-trial variability in event-related BOLD signals. 15, 823-835.

Duvernoy, H.M., Delon, S., Vannson, J.J.B.r.b., 1981. Cortical blood vessels of the human brain. 7, 519-579.

Finn, E.S., Huber, L., Jangraw, D.C., Molfese, P.J., Bandettini, P.A.J.N.n., 2019. Layer-dependent activity in human prefrontal cortex during working memory. 22, 1687-1695.

Francis, C., Frederic, L., Sylvie, L., Prasanna, P., Henri, D.J.M., 2009. Scaling laws for branching vessels of human cerebral cortex. 16, 331-344.

Gagnon, L., Sakadžić, S., Lesage, F., Musacchia, J.J., Lefebvre, J., Fang, Q., Yücel, M.A., Evans, K.C., Mandeville, E.T., Cohen-Adad, J.J.J.o.N., 2015. Quantifying the

595 microvascular origin of BOLD-fMRI from first principles with two-photon microscopy
596 and an oxygen-sensitive nanoprobe. 35, 3663-3675.
597 Gao, Y.-R., Greene, S.E., Drew, P.J.J.N., 2015. Mechanical restriction of intracortical
598 vessel dilation by brain tissue sculpts the hemodynamic response. 115, 162-176.
599 Genois, É., Gagnon, L., Desjardins, M.J.M.R.i.M., 2020. Modeling of vascular space
600 occupancy and BOLD functional MRI from first principles using real microvascular
601 angiograms. 85, 456-468.
602 Goense, J., Merkle, H., Logothetis, N.K., 2012. High-resolution fMRI reveals laminar
603 differences in neurovascular coupling between positive and negative BOLD
604 responses. Neuron 76, 629-639.
605 Goense, J.B., Logothetis, N.K., 2006. Laminar specificity in monkey V1 using high-
606 resolution SE-fMRI. Magnetic resonance imaging 24, 381-392.
607 Griffeth, V.E., Simon, A.B., Buxton, R.B.J.N., 2015. The coupling of cerebral blood
608 flow and oxygen metabolism with brain activation is similar for simple and complex
609 stimuli in human primary visual cortex. 104, 156-162.
610 Griswold, M.A., Jakob, P.M., Heidemann, R.M., Nittka, M., Jellus, V., Wang, J., Kiefer,
611 B., Haase, A.J.M.R.i.M.A.O.J.o.t.I.S.f.M.R.i.M., 2002. Generalized autocalibrating
612 partially parallel acquisitions (GRAPPA). 47, 1202-1210.
613 Grubb, R.L., Raichle, M.E., Eichling, J.O., Ter-Pogossian, M.M., 1974. The effects of
614 changes in PaCO2 cerebral blood volume, blood flow, and vascular mean transit time.
615 Stroke 5, 630-639.
616 Handwerker, D.A., Ollinger, J.M., D'Esposito, M.J.N., 2004. Variation of BOLD
617 hemodynamic responses across subjects and brain regions and their effects on
618 statistical analyses. 21, 1639-1651.
619 Havlicek, M., Uludag, K.J.B., 2019. A dynamical model of the laminar BOLD response.
620 609099.
621 Heinzle, J., Koopmans, P.J., den Ouden, H.E., Raman, S., Stephan, K.E.J.N., 2016.
622 A hemodynamic model for layered BOLD signals. 125, 556-570.
623 Hua, J., Liu, P., Kim, T., Donahue, M., Rane, S., Chen, J.J., Qin, Q., Kim, S.-G.J.N.,
624 2019. MRI techniques to measure arterial and venous cerebral blood volume. 187,
625 17-31.
626 Hua, J., Qin, Q., Donahue, M.J., Zhou, J., Pekar, J.J., van Zijl, P., 2011. Inflow-based
627 vascular-space-occupancy (iVASO) MRI. Magnetic resonance in medicine 66, 40-56.
628 Huber, L., 2011. Magnetic resonance imaging method for measuring functional
629 cerebral blood volume changes at 7 Tesla. Methods and Development Unit Nuclear
630 Magnetic Resonance, MPI for Human ….
631 Huber, L., 2014. Mapping Human Brain Activity by Functional Magnetic Resonance
632 Imaging of Blood Volume.
633 Huber, L., Goense, J., Ivanov, D., Krieger, S., Turner, R., Moeller, H.E., 2013. Cerebral
634 blood volume changes in negative BOLD regions during visual stimulation in humans
635 at 7T. 21st Annual Meeting of the International Society for Magnetic Resonance in
636 Medicine.
637 Huber, L., Goense, J., Kennerley, A.J., Trampel, R., Guidi, M., Reimer, E., Ivanov, D.,
638 Neef, N., Gauthier, C.J., Turner, R., 2015. Cortical lamina-dependent blood volume
639 changes in human brain at 7 T. Neuroimage 107, 23-33.
640 Huber, L., Handwerker, D.A., Jangraw, D.C., Chen, G., Hall, A., Stüber, C., Gonzalez-
641 Castillo, J., Ivanov, D., Marrett, S., Guidi, M., 2017. High-resolution CBV-fMRI allows
642 mapping of laminar activity and connectivity of cortical input and output in human M1.
643 Neuron 96, 1253-1263. e1257.

Huber, L., Ivanov, D., Handwerker, D.A., Marrett, S., Guidi, M., Uludağ, K., Bandettini, P.A., Poser, B.A., 2016. Techniques for blood volume fMRI with VASO: from low-resolution mapping towards sub-millimeter layer-dependent applications. Neuroimage.

Huber, L., Ivanov, D., Krieger, S.N., Streicher, M.N., Mildner, T., Poser, B.A., Möller, H.E., Turner, R., 2014. Slab-selective, BOLD-corrected VASO at 7 Tesla provides measures of cerebral blood volume reactivity with high signal-to-noise ratio. Magnetic resonance in medicine 72, 137-148.

Huber, L.R., Poser, B.A., Bandettini, P.A., Arora, K., Wagstyl, K., Cho, S., Goense, J., Nothnagel, N., Morgan, A.T., Van Den Hurk, J.J.B., 2020. LAYNII: A software suite for layer-fMRI.

Jahanian, H., Peltier, S., Noll, D.C., Hernandez Garcia, L.J.M.R.i.M., 2015. Arterial cerebral blood volume–weighted functional MRI using pseudocontinuous arterial spin tagging (AVAST). 73, 1053-1064.

Jin, T., Kim, S.-G., 2006. Spatial dependence of CBV-fMRI: a comparison between VASO and contrast agent based methods. 2006 International Conference of the IEEE Engineering in Medicine and Biology Society. IEEE, pp. 25-28.

Jin, T., Kim, S.-G., 2008a. Improved cortical-layer specificity of vascular space occupancy fMRI with slab inversion relative to spin-echo BOLD at 9.4 T. Neuroimage 40, 59-67.

Jin, T., Kim, S.-G.J.N., 2008b. Cortical layer-dependent dynamic blood oxygenation, cerebral blood flow and cerebral blood volume responses during visual stimulation. 43, 1-9.

Kashyap, S., Ivanov, D., Havlicek, M., Poser, B., Uludag, K., 2016. High-resolution T1-mapping using inversion-recovery EPI and application to cortical depth-dependent fMRI at 7 Tesla. Proceedings of the 24th Annual Meeting of ISMRM, Singapore.

Kim, S.G., Hendrich, K., Hu, X., Merkle, H., Uğurbil, K.J.N.i.B., 1994. Potential pitfalls of functional MRI using conventional gradient-recalled echo techniques. 7, 69-74.

Kim, T., Hendrich, K.S., Masamoto, K., Kim, S.-G.J.J.o.C.B.F., Metabolism, 2007. Arterial versus total blood volume changes during neural activity-induced cerebral blood flow change: implication for BOLD fMRI. 27, 1235-1247.

Kim, T., Kim, S.-G., 2010. Cortical layer-dependent arterial blood volume changes: improved spatial specificity relative to BOLD fMRI. Neuroimage 49, 1340-1349.

Kim, T., Kim, S.-G.J.J.o.C.B.F., Metabolism, 2011a. Temporal dynamics and spatial specificity of arterial and venous blood volume changes during visual stimulation: implication for BOLD quantification. 31, 1211-1222.

Kim, T., Kim, S.-G.J.T.o.n.j., 2011b. Suppl 1: Quantitative MRI of Cerebral Arterial Blood Volume. 5, 136.

Koopmans, P.J., Barth, M., Norris, D.G., 2010. Layer-specific BOLD activation in human V1. Human brain mapping 31, 1297-1304.

Koopmans, P.J., Barth, M., Orzada, S., Norris, D.G.J.N., 2011. Multi-echo fMRI of the cortical laminae in humans at 7 T. 56, 1276-1285.

Lauwers, F., Cassot, F., Lauwers-Cances, V., Puwanarajah, P., Duvernoy, H.J.N., 2008. Morphometry of the human cerebral cortex microcirculation: general characteristics and space-related profiles. 39, 936-948.

Lawrence, S.J., Norris, D.G., De Lange, F.P.J.E., 2019. Dissociable laminar profiles of concurrent bottom-up and top-down modulation in the human visual cortex. 8, e44422.

Light, K.C., Turner, J.R., Hinderliter, A.L., Sherwood, A.J.H.P., 1993. Race and gender comparisons: I. Hemodynamic responses to a series of stressors. 12, 354.

694 Lu, H., Golay, X., Pekar, J.J., van Zijl, P., 2003. Functional magnetic resonance
695 imaging based on changes in vascular space occupancy. Magnetic resonance in
696 medicine 50, 263-274.
697 Ma, Y., Shaik, M.A., Kim, S.H., Kozberg, M.G., Thibodeaux, D.N., Zhao, H.T., Yu, H.,
698 Hillman, E.M.J.P.T.o.t.R.S.B.B.S., 2016. Wide-field optical mapping of neural activity
699 and brain haemodynamics: considerations and novel approaches. 371, 20150360.
700 Markuerkiaga, I., Barth, M., Norris, D.G., 2016. A cortical vascular model for examining
701 the specificity of the laminar BOLD signal. Neuroimage 132, 491-498.
702 Marques, J.P., Kober, T., Krueger, G., van der Zwaag, W., Van de Moortele, P.-F.,
703 Gruetter, R.J.N., 2010. MP2RAGE, a self bias-field corrected sequence for improved
704 segmentation and T1-mapping at high field. 49, 1271-1281.
705 O'Brien, K.R., Magill, A.W., Delacoste, J., Marques, J.P., Kober, T., Fautz, H.P.,
706 Lazeyras, F., Krueger, G.J.J.o.M.R.I., 2014. Dielectric pads and low-adiabatic pulses:
707 Complementary techniques to optimize structural T1w whole-brain MP2RAGE scans
708 at 7 tesla. 40, 804-812.
709 Obata, T., Liu, T.T., Miller, K.L., Luh, W.-M., Wong, E.C., Frank, L.R., Buxton, R.B.J.N.,
710 2004. Discrepancies between BOLD and flow dynamics in primary and supplementary
711 motor areas: application of the balloon model to the interpretation of BOLD transients.
712 21, 144-153.
713 Ogawa, S., Lee, T.M., Nayak, A.S., Glynn, P., 1990. Oxygenation-sensitive contrast
714 in magnetic resonance image of rodent brain at high magnetic fields. Magnetic
715 resonance in medicine 14, 68-78.
716 Olman, C.A., Harel, N., Feinberg, D.A., He, S., Zhang, P., Ugurbil, K., Yacoub, E.,
717 2012. Layer-specific fMRI reflects different neuronal computations at different depths
718 in human V1. PloS one 7, e32536.
719 Petridou, N., Siero, J.C.J.N., 2017. Laminar fMRI: What can the time domain tell us?
720 Polimeni, J.R., Fischl, B., Greve, D.N., Wald, L.L.J.N., 2010. Laminar analysis of 7 T
721 BOLD using an imposed spatial activation pattern in human V1. 52, 1334-1346.
722 Polimeni, J.R., Hinds, O.P., Balasubramanian, M., van der Kouwe, A., Wald, L.L.,
723 Dale, A.M., Fischl, B., Schwartz, E.L., 2005. The human V1–V2–V3 visuotopic map
724 complex measured via fMRI at 3 and 7 Tesla.
725 Polimeni, J.R., Renvall, V., Zaretskaya, N., Fischl, B.J.N., 2018. Analysis strategies
726 for high-resolution UHF-fMRI data. 168, 296-320.
727 Poplawsky, A.J., Fukuda, M., Murphy, M., Kim, S.-G.J.J.o.N., 2015. Layer-specific
728 fMRI responses to excitatory and inhibitory neuronal activities in the olfactory bulb.
729 35, 15263-15275.
730 Poplawsky, A.J., Kim, S.-G.J.N., 2014. Layer-dependent BOLD and CBV-weighted
731 fMRI responses in the rat olfactory bulb. 91, 237-251.
732 Poser, B.A., Koopmans, P.J., Witzel, T., Wald, L.L., Barth, M., 2010. Three
733 dimensional echo-planar imaging at 7 Tesla. Neuroimage 51, 261-266.
734 Ress, D., Glover, G.H., Liu, J., Wandell, B.J.n., 2007. Laminar profiles of functional
735 activity in the human brain. 34, 74-84.
736 Schmid, F., Barrett, M.J., Jenny, P., Weber, B.J.N., 2017. Vascular density and
737 distribution in neocortex.
738 Shih, Y.-Y.I., Chen, Y.-Y., Lai, H.-Y., Kao, Y.-C.J., Shyu, B.-C., Duong, T.Q.J.N., 2013.
739 Ultra high-resolution fMRI and electrophysiology of the rat primary somatosensory
740 cortex. 73, 113-120.
741 Silva, A.C., Koretsky, A.P.J.P.o.t.N.A.o.S., 2002. Laminar specificity of functional MRI
742 onset times during somatosensory stimulation in rat. 99, 15182-15187.

743 Stephan, K., Petzschner, F., Kasper, L., Bayer, J., Wellstein, K., Stefanics, G.,
744 Pruessmann, K., Heinzle, J., 2017. Laminar fMRI and computational theories of brain
745 function. Neuroimage.
746 Turner, R.J.N., 2002. How much cortex can a vein drain? Downstream dilution of
747 activation-related cerebral blood oxygenation changes. 16, 1062-1067.
748 Uludağ, K., Müller-Bierl, B., Uğurbil, K.J.N., 2009. An integrative model for neuronal
749 activity-induced signal changes for gradient and spin echo functional imaging. 48,
750 150-165.
751 Van Kerkoerle, T., Self, M.W., Roelfsema, P.R.J.N.c., 2017. Layer-specificity in the
752 effects of attention and working memory on activity in primary visual cortex. 8, 1-14.
753 Vanzetta, I., Hildesheim, R., Grinvald, A.J.J.o.N., 2005. Compartment-resolved
754 imaging of activity-dependent dynamics of cortical blood volume and oximetry. 25,
755 2233-2244.
756 Vazquez, A.L., Fukuda, M., Kim, S.-G.J.J.o.C.B.F., Metabolism, 2012. Evolution of the
757 dynamic changes in functional cerebral oxidative metabolism from tissue mitochondria
758 to blood oxygen. 32, 745-758.
759 Waehnert, M., Dinse, J., Weiss, M., Streicher, M.N., Waehnert, P., Geyer, S., Turner,
760 R., Bazin, P.-L.J.N., 2014. Anatomically motivated modeling of cortical laminae. 93,
761 210-220.
762 Weber, B., Keller, A.L., Reichold, J., Logothetis, N.K., 2008. The microvascular system
763 of the striate and extrastriate visual cortex of the macaque. Cerebral cortex 18, 2318-
764 2330.
765 Yablonskiy, D.A., Haacke, E.M., 1994. Theory of NMR signal behavior in magnetically
766 inhomogeneous tissues: the static dephasing regime. Magnetic resonance in medicine
767 32, 749-763.
768 Yu, X., Qian, C., Chen, D.-y., Dodd, S.J., Koretsky, A.P.J.N.m., 2014. Deciphering
769 laminar-specific neural inputs with line-scanning fMRI. 11, 55.
770 Zhang, X., Petersen, E.T., Ghariq, E., De Vis, J., Webb, A., Teeuwisse, W.M.,
771 Hendrikse, J., Van Osch, M.J.M.r.i.m., 2013. In vivo blood T1 measurements at 1.5 T,
772 3 T, and 7 T. 70, 1082-1086.
773 Zhao, F., Wang, P., Hendrich, K., Ugurbil, K., Kim, S.-G.J.N., 2006. Cortical layer-
774 dependent BOLD and CBV responses measured by spin-echo and gradient-echo
775 fMRI: insights into hemodynamic regulation. 30, 1149-1160.
776 Zweifach, B.W., Lipowsky, H.H.J.C.r., 1977. Quantitative studies of microcirculatory
777 structure and function. III. Microvascular hemodynamics of cat mesentery and rabbit
778 omentum. 41, 380-390.

779